Identifying dynamic, partially occupied residues using anomalous scattering

Serena Rocchio, Ramona Duman, Kamel El Omari, Vitaliy Mykhaylyk, Christian Orr, Zhen Yan, Loïc Salmon, Armin Wagner, James Bardwell, Scott Horowitz

Identifying dynamic, partially occupied residues using anomalous scattering

Serena Rocchio,[a,b] Ramona Duman,[c,d] Kamel El Omari,[c,d] Vitaliy Mykhaylyk,[c,d] Christian Orr, [c,d] Zhen Yan,[a] Loïc Salmon[e], Armin Wagner,[c,d]* James C. A. Bardwell[a]* and Scott Horowitz[f]*

[a]**Department of Molecular, Cellular and Developmental Biology, and the Howard Hughes Medical Institute, University of Michigan, Ann Arbor, MI 48109, USA**

[b]**Department of Biochemical Sciences "A Rossi Fanelli", Sapienza University of Roma, 00185, Rome, Italy**

[c]**Diamond Light Source Ltd, Diamond House, Harwell Science and Innovation Campus, Didcot OX11 0DE, England**

[d]**Research Complex at Harwell, Rutherford Appleton Laboratory, Harwell Oxford, Didcot OX11 0FA, United Kingdom.**

[e]**Centre de RMN à Très Hauts Champs, CNRS, ENS Lyon, UCB Lyon 1, Université de Lyon, 69100 Villeurbanne, France**

[f]**Department of Chemistry & Biochemistry and the Knoebel Institute for Healthy Aging, University of Denver, Denver, CO 80208, USA**

*Correspondence emails: AW: armin.wagner@diamond.ac.uk; JCAB: jbardwel@umich.edu; SH: Scott.Horowitz@du.edu

Keywords: Anomalous scattering, crystallography, protein dynamics, chaperone, protein folding

Synopsis: Structural studies on partially occupied, heterogeneous protein systems by crystallography are difficult. We present methods here for detecting these states in crystals.

Abstract

Although often presented as taking single “snapshots” of a protein’s conformation, X-ray crystallography provides an averaged structure over time and space within the crystal. The important but difficult task of characterizing structural ensembles in crystals is typically limited to small conformational changes, such as multiple side-chain conformations. A crystallographic method was recently introduced that utilizes Residual Electron and Anomalous Density (READ) to characterize structural ensembles encompassing large-scale structural changes. Key to this method is an ability to accurately measure anomalous signals and distinguish them from noise or other anomalous scatterers. This report presents an optimized data collection and analysis strategy for partially occupied iodine anomalous signals. Using the long wavelength-optimized beamline I23 at Diamond Light Source, the ability to accurately distinguish the positions of anomalous scatterers with as low as ~12% occupancy is demonstrated. The number and position of these anomalous scatterers are consistent with previous biophysical, kinetic and structural data that suggest the protein Im7 binds to the chaperone Spy in multiple partially occupied conformations. Finally, READ selections demonstrate that re-measured data with the new protocols are consistent with our previously characterized structural ensemble of the chaperone Spy with its client Im7. This study shows that a long-wavelength beamline results in easily validated anomalous signals that are strong enough to be used to detect and characterize highly disordered sections of crystal structures.

1. Introduction

In crystallography, anomalous scattering is commonly used to help solve the phase problem (Hendrickson, 2014). A second, less well-utilized aspect of anomalous scattering is its ability to selectively label and identify residues of interest. Crystallographers can use anomalous maps to pinpoint metal ions (Handing *et al.*, 2018) or to aid in model building or electron density interpretation (Pflug *et al.*, 2012; Wang *et al.*, 2012). We recently introduced a method called READ that uses anomalous maps to allow the reconstruction of highly heterogeneous conformational ensembles in regions of the protein that are not well ordered enough for traditional model building (Salmon *et al.*, 2018; Horowitz *et al.*, 2016). This method uses selective anomalous labeling with iodo-phenylalanine (pI-Phe) to generate multiple partially occupied iodine anomalous signals in the crystal corresponding to different protein conformations. Ensemble selection techniques (Venditti *et al.*, 2016; Salmon *et al.*, 2018; Horowitz *et al.*, 2016) are then used to create ensembles that are consistent with both the anomalous data and weak electron density data for the disordered segment(s) of the crystal. The Im7 ensembles generated by READ were highly consistent with orthogonal experimental approaches also used to characterize Im7 binding and folding with Spy, including NMR spectroscopy, thermodynamic, and kinetic analyses (Salmon *et al.*, 2018; Horowitz *et al.*, 2016; Koldewey *et al.*, 2016; Stull *et al.*, 2016; He & Hiller, 2018; He *et al.*, 2016).

A critical step in the READ process is the correct identification of weak anomalous signals (Horowitz, Salmon, *et al.*, 2018; Wang, 2018). Selective labeling requires tunable X-ray sources to achieve high levels of anomalous scattering for particular atoms (Phillips *et al.*, 1976). However, many important anomalous scatterers do not have their K and L absorption edges within wavelength ranges of standard synchrotron beamlines for macromolecular crystallography, resulting in weak anomalous signals. Recently, a novel beamline, I23 at Diamond Light Source, was introduced to collect anomalous data at substantially longer wavelengths than was previously possible. The I23 beamline operates in an in-vacuum sample environment and features a number of other innovations that make it optimal for anomalous data collection (Wagner *et al.*, 2016). Here, we present an optimized data collection strategy for identification of iodine anomalous scattering positions that greatly improves our ability to detect weak and partially occupied states in

crystals. Co-crystals of the chaperone Spy with its disordered client Im7 were used to collect anomalous data for three iodine-containing Im7 mutants. Using multiple wavelengths and collections from different orientations obtained with a multi-axis goniometer, we demonstrate that it is possible to detect the iodine signal even at low occupancy and clearly distinguish it from other anomalous scatterers. The anomalous signals indicate that Im7 binds to Spy in multiple conformations along its concave surface, consistent with findings from other biophysical investigations (Salmon *et al.*, 2018; Horowitz *et al.*, 2016). These data were used in a new READ selection, which yields results consistent with our previously determined structural ensemble (Horowitz *et al.*, 2016). The data demonstrate the feasibility of using anomalous scatterers as an approach to understand disordered systems in crystallography.

2. Methods

2.1. Crystallization

The super Spy chaperone mutant, Spy H96L (Quan *et al.*, 2014), was used here for co-crystallization experiments, as we found it formed crystals more readily than wild-type Spy protein (Horowitz *et al.*, 2016). Spy-Im7 co-crystals were obtained using the vapor diffusion technique and the crystallization conditions 22–34% PEG 3000, 70–270 m*M* zinc acetate, and 0.1 *M* imidazole, pH 8.0. Crystallization was performed using 15–50 mg/ml Spy H96L, with Im7 peptides that represent the 6–26 portion of the Im7 peptide in a 1:1–1:2 ratio. The Im7 peptides (^{6}SISDYTEAEFVQLLKEIEKEN^{26}) used here for the co-crystallization experiments have a single iodo-phenylalanine substitution in one of the positions 18, 19, and 20, respectively. Of note, we previously found that in these conditions, Spy and its mutants only forms diffraction-quality crystals in the presence of clients (casein and Im7 were previously tested), precluding the use of soaks (Horowitz *et al.*, 2016).

2.1.1. Crystal harvesting. Crystals were cryoprotected by increasing the PEG 3000 concentration up to 35% and flash frozen in liquid nitrogen. Crystals were harvested using LithoLoop sample mounts (Molecular Dimensions, Newmarket, UK) matched to the size of the crystal, glued to copper pins as part of the dedicated I23 sample holder assembly, optimized for cryogenic sample transfer and storage in the beamline vacuum environment.

2.1.2. Data collection. Data were collected at beamline I23 at Diamond Light Source at X-ray energies of 5.2 and 4.5 keV, above and below the iodine L absorption edges ($E_{L(I)}$ = 5.188 keV, $E_{L(II)}$ = 4.852 keV, $E_{L(III)}$ = 4.557 keV) using the semi-cylindrical PILATUS 12*M* area detector. For each data set, 360° of data were collected with an exposure time of 0.1 sec per 0.1° rotation in inverse beam setting of 20° wedges. Taking advantage of the multi-axis goniometer, data were collected at 5.2 keV at different κ and φ goniometer angles (Table 1). To identify the remaining anomalously scattering ligands, the zinc and chloride ions, two additional sets of data were collected for the Spy:Im7-L19pI-Phe complex at 2.87 and 2.75 keV.

2.1.3. Model building and refinement. Data integration and scaling were performed with *XDS* (Kabsch, 2010) and *AIMLESS* (Evans & Murshudov, 2013), respectively. Phased anomalous difference Fourier maps were calculated using *ANODE* (Thorn & Sheldrick, 2011). Molecular replacement was performed using the known structure of the Spy-Im7 complex (PDB entry 5wnw) as the search model in *Phenix* (Adams *et al.*, 2010). Model building and refinement were accomplished using *Coot* (Emsley *et al.*, 2010) and *Phenix* (Afonine *et al.*, 2012), respectively. Iodine atoms were placed into the peaks of the phased anomalous difference Fourier maps produced by *ANODE*. To test the stability and

reproducibility of the iodine occupancy and atomic displacement parameter (ADP) refinements, we followed the protocol described in (Langan *et al.*, 2018). In total, 10,000 models with randomly assigned starting values were created using phenix.pdb_tools. 50 cycles of refinement using phenix.refine were performed with fixed XYZ coordinates refining only the occupancies and ADPs. The values as used in the final coordinate files were then based on the analysis of 2D-histograms for the individual atoms. The protein structures were very similar in each case, with the maximum C_α root-mean-square deviation (r.m.s.d.) = 0.41 Å between protein structures.

2.1.4. Dose estimation. The absorbed dose was estimated for each crystal by using the program RADDOSE-3D (Bury *et al.*, 2018). RADDOSE-3D calculates the dose absorbed by a crystal in an X-ray beam as function of the beam characteristics (wavelength, flux, profile and size), crystal properties (unit cell, size, amino acid and solvent composition) and data collection strategy (number of images, oscillation range, exposure time). The cumulative dose was estimated for those crystals submitted to multiple and sequential data collections.

2.2. READ ensemble selection. The previously described READ selection procedure was used to select an ensemble of structures to fit the weak residual density and the iodine anomalous signals (Salmon *et al.*, 2018; Horowitz *et al.*, 2016). In order to obtain sufficient experimental information, we combined previous crystallography datasets of Spy and Im7 6-45 (dataset 1), both for the residual electron density and the iodine signals, with the data presented here (dataset 2). All selections include: the electronic density from dataset 1, the iodine anomalous signals from dataset 1 except those arising from L19pI-Phe, and a variable combination (described in the main text) of iodine anomalous signals arising from L18pI-Phe (dataset 2), L19pI-Phe (dataset 1 or 2) or K20pI-Phe (dataset 2). To test the predictive power of the ensemble and the coherence of the dataset, some iodine anomalous signals not used in the fit were back-predicted from the final ensemble. The initial conformational pool, and the binning of the electron density were identical to our previous study, as well as the parameters used in the selection procedure (Salmon *et al.*, 2018; Horowitz *et al.*, 2016). This procedure was chosen to ensure that potential deviations between the two studies would arise only from the newly recorded iodine dataset.

2.3. Isothermal titration calorimetry. Binding affinity of SpyH96L to Im7 6-26 peptides was determined by isothermal titration calorimetry (ITC) using a MicroCal iTC200 instrument (Malvern). The thermodynamic parameters upon titration of Spy H96L (1.25 m*M*) to Im7 6-26 peptides (0.11 µ*M* for the wild type, 0.055 µ*M* for Im7 6–26 L18pI-Phe, L19pI-Phe, and K20pI-Phe peptides) were measured at 10 °C in a buffer containing 40 mM HEPES-NaOH pH 7.5, 100 mM NaCl. For each experiment, an injection volume of 2 µl was used at intervals of 180 s. ITC thermograms were fit to a one-site model using the Origin software provided with the instrument. The Im7 6–26 peptide binds to Spy H96L with a 7.8 ± 0.6 µ*M* dissociation constant, which is similar to the dissociation constant of a partially folded variant of Im7 for wild-type Spy. The Im7 6–26 L18pI-Phe, L19pI-Phe, and K20pI-Phe peptides bind to Spy H96L with dissociation constants in the same range of Im7 6-26 peptide wild type (Fig. S1).

3. Results

3.1. Data collection strategy

Spy is one of a group of chaperones that allows clients to fold while remaining continuously bound to the chaperone's surface (Horowitz, Koldewey, *et al.*, 2018). We have previously observed that the chaperone substrate Im7 exists in a heterogeneous, largely disordered crystallographic ensemble while bound to the chaperone Spy (Horowitz *et al.*, 2016). To refine strategies for detecting anomalous scattering for observing partially occupied disordered states, we co-crystallized the tight-binding Spy H96L variant with short peptides derived from its client, Im7. These peptides each had a single iodo-phenylalanine substitution at positions 18, 19, and 20, respectively.

Our data collection strategy was geared to determine the positions of these iodines with maximum sensitivity while ensuring that the signals were due to iodine and not from other weak anomalous scatterers present in the crystal. To maximize signal intensity, we selected data collection wavelengths that should give complementary data based on the change of anomalous scattering around the iodine L-edges (Fig. S2). We collected data primarily at λ = 2.3843 Å (*E* = 5.2 keV), just above the L(I) absorption edge of iodine, as well as below the L(III) edge at λ = 2.7552 Å (*E* = 4.5 keV). At these two energies, the anomalous contributions *f*" to the scattering factor differ by a factor of 3.9 ($f''_{4.5keV}$ = 3.42 e- vs. $f''_{5.2keV}$ = 13.41 e-). By collecting in this fashion, we reasoned that we should be able to specifically distinguish iodine anomalous signals from other elements by analyzing the resulting phased anomalous difference Fourier maps. Peaks that are present in the higher energy dataset (above the iodine edge) (λ = 2.3843 Å, *E* = 5.2 keV), but absent in the lower energy dataset (below the iodine edge) (λ = 2.7552 Å, 4.5 keV) originate from iodine atoms. We further reasoned that one of the best ways to distinguish noise from real signals is to show that the same anomalous signal exists in independent datasets collected at different crystal orientations. We thus collected datasets at λ = 2.3843 Å (*E* = 5.2 keV) from different goniometer κ angles (κ = −40°, φ = −70° and κ = −20°, φ = −70°) so we could compare and stringently determine the number and positions of the iodine peaks. Finally, when possible, we compared data from multiple crystals with the same components to see the reproducibility of the anomalous signals. To help identify zinc and chlorine sites in the crystal, we also collected datasets at λ = 4.3200 Å (*E* = 2.87 keV) and λ = 4.5085 Å (*E* = 2.75 keV), just above and below the chlorine K absorption edge (*E* = 2.822 keV), respectively. Despite the very long wavelengths, the data quality was good enough to observe the peaks expected for chlorine and zinc ions (Table 3, Fig. S3). To our knowledge, these are the first protein crystallography datasets collected around the chlorine absorption edge.

For initial inspection of the 5.2 keV phased anomalous difference Fourier maps calculated with initial phases from molecular replacement, a cut off of 4 σ was used, based on the *ANODE* recommendations. Using refined, final model phases, all putative peaks that were present in the 5.2 keV map above 4 σ increased to be at least 6 σ, and where possible the threshold was set as high as possible. For example, in the L19pI-Phe data collection, that shown several low occupancy anomalous signals, the *ANODE* anomalous peaks were analyzed with a cut off at 6 σ to ensure confidence in assigning the anomalous signals beyond the noise level (Fig. S5).

It is generally accepted that the rate of radiation damage in protein crystals is proportional to the dose. Here, the effect of radiation damage on crystals has been investigated by monitoring a number of parameters as a function of the absorbed dose (Table S1). For each dataset, the absorbed dose was estimated using knowledge on the incident beam characteristic (energy, flux, size) and the crystal characteristics (volume, morphology, unit cell size, protein atomic content, number of amino acids, and solvent composition), as well as the exposure time per image and total number of images. In case

of multiple and sequential datasets collected on the same crystal, the cumulative dose was evaluated.

Table 1. Data Collection and processing. Values for the outer shell are given in parentheses. All space groups are $P4_122$

	L18pI-Phe	L18pI-Phe 2nd dataset (κ: -40°, φ: -70°)	L19pI-Phe 1st crystal	L19pI-Phe 1st crystal	L19pI-Phe 1st crystal, 2nd dataset (κ: -20°, φ: -70°)	L19pI-Phe 1st crystal	L19pI-Phe 1st crystal
Wavelength (Å)	2.3843	2.3843	2.3843	2.7552	2.3843	4.5085	4.3200
a, *b*, *c* (Å)	42.80 42.80 253.78	42.87 42.87 253.97	43.02 43.02 257.15	43.01 43.01 256.91	43.09 43.09 257.62	43.16 43.16 257.96	43.19 43.19 258.46
α, β, γ (°)	90.00 90.00 90.00	90.00 90.00 90.00	90.00 90.00 90.00	90.00 90.00 90.00	90.00 90.00 90.00	90.00 90.00 90.00	90.00 90.00 90.00
Resolution range (Å)	42.30-2.11(2.1-2.06)	42.33 - 2.23 (2.29-2.23)	43.02-2.00(2.05-2.00)	43.01-2.01(2.06-2.01)	42.94-2.11 (2.16-2.11)	43.16 –2.95 (3.03-2.95)	43.08-2.82 (2.90-2.82)
Total No. of reflections	233502 (12906)	192411 (9558)	257104 (14125)	221870 (12079)	231087 (12741)	58977 (1694)	67203 (1798)
No. of unique reflections	15755 (1112)	12296 (826)	17581 (1283)	17223 (1221)	14660 (991)	5755 (389)	6518 (413)
R_{merge} (%)	0.064 (1.822)	0.115 (1.935)	0.056 (1.794)	0.057 (2.093)	0.065 (1.619)	0.165 (0.816)	0.158 (1.043)
$R_{p.i.m.}$ (%)	0.016 (0.544)	0.028 (0.586)	0.014 (0.543)	0.014 (0.673)	0.016 (0.454)	0.048 (0.403)	0.044 (0.518)
$\langle I/\sigma(I) \rangle$	21.0 (1.4)	14.6 (1.2)	26.2 (1.4)	22.8 (1.00)	23.7 (1.5)	10.1 (1.6)	10.4 (1.0)
CC (1/2)	1.000 (0.512)	0.997 (0.520)	0.999 (0.552)	0.999 (0.478)	0.998 (0.647)	0.993 (0.604)	0.992 (0.523)
Completeness (%)	99.9 (99.9)	98.4 (95.1)	100.0 (100.0)	99.7 (99.1)	97.1 (90.9)	98.8 (93.4)	98.6 (88.7)

Overall *B* factor from Wilson plot ($Å^2$)	47.12	52.82	46.08	49.06	52.68	89.78	90.89
Anomalous Completeness	99.8 (98.2)	98.3 (94.0)	99.9 (100.0)	99.6 (99.2)	96.0 (89.2)	97.8 (89.2)	97.9 (86.7)
Anomalous Multiplicity	8.2 (6.3)	8.7 (6.2)	7.9 (5.7)	6.9 (5.1)	8.7 (7.0)	5.6 (2.4)	5.5 (2.3)

	L19pI-Phe 2nd crystal	L19pI-Phe 2nd crystal, 2nd dataset (κ: -40°, φ: -70°)	L19pI-Phe 3rd crystal	L19pI-Phe 4th crystal	K20pI-Phe 1st crystal	K20pI-Phe 1st crystal	K20pI-Phe 1st crystal, 2nd dataset (κ: -20°, φ: -70°)
Wavelength (Å)	2.3843	2.3843	2.3843	2.3843	2.3843	2.7552	2.3843
a, *b*, *c* (Å)	43.01 43.01 259.27	43.12 43.12 259.86	42.95 42.95 256.87	42.80 42.80 253.90	42.84 42.84 257.63	42.86 42.86 257.51	42.91 42.91 258.00
α, β, γ (°)	90.00 90.00 90.00	90.00 90.00 90.00	90.00 90.00 90.00	90.00 90.00 90.00	90.00 90.00 90.00	90.00 90.00 90.00	90.00 90.00 90.00
Resolution range (Å)	43.01-2.18 (2.24-2.18)	43.31-2.35 (2.42-2.35)	22.05-2.85 (2.92-2.85)	42.32-3.25 (3.34-3.25)	42.84-2.07 (2.12-2.07)	42.86-2.13 (2.19-2.13)	42.91-2.23 (2.23-2.29)
Total No. of reflections	215289 (11599)	182649 (10469)	81739 (4032)	52884 (2353)	222445 (11148)	176931(8429)	157318 (8988)
No. of unique reflections	13508 (931)	11184 (801)	5570 (295)	3982 (229)	15762 (1115)	14248 (1015)	11268 (880)
R_{merge} (%)	0.084 (3.695)	0.078 (1.514)	0.093 (1.477)	0.114 (1.181)	0.080 (1.483)	0.083 (2.003)	0.075 (1.815)
$R_{p.i.m.}$ (%)	0.021 (1.055)	0.019 (0.424)	0.024 (0.386)	0.030 (0.335)	0.020 (0.455)	0.022 (0.669)	0.019 (0.548)
$\langle I/\sigma(I) \rangle$	18.9 (0.7)	21.2 (1.6)	19.2 (1.2)	14.6 (1.8)	18.9 (1.4)	16.8 (1.2)	17.0 (1.4)
CC (1/2)	0.999 (0.623)	0.998 (0.763)	0.999 (0.673)	0.998 (0.583)	0.997 (0.582)	0.999 (0.453)	1.000 (0.568)
Completeness (%)	97.8 (94.1)	99.8 (100.0)	87.5 (66.6)	92.9 (75.0)	99.7 (98.3)	97.8 (98.9)	87.6 (97.0)
Overall *B* factor from Wilson plot (Å^2)	46.47	56.13	79.59	89.38	43.20	47.49	50.23

Anomalous Completeness	97.0 (91.6)	99.8 (100.0)	81.8 (61.1)	85.5 (67.8)	98.7 (94.9)	96.2 (97.1)	83.2 (93.8)
Anomalous Multiplicity	8.8 (6.6)	9.0 (6.9)	14.7 (13.7)	7.9 (6.0)	7.7 (5.3)	6.6 (4.3)	7.5 (5.5)

	K20pI-Phe 2nd crystal	K20pI-Phe 3rd crystal	K20pI-Phe 4th crystal
Wavelength (Å)	2.3843	2.3843	2.3843
a, *b*, *c* (Å)	42.99 42.99 259.38	42.69 42.69 255.89	42.59 42.59 254.90
α, ß, γ (°)	90.00 90.00 90.00	90.00 90.00 90.00	90.00 90.00 90.00
Resolution range (Å)	43.23-2.10 (2.15-2.10)	42.65-2.19 (2.25-2.19)	42.48 (3.34 (3.43-3.34)
Total No. of reflections	199534 (9497)	211390 (12146)	53111 (2492)
No. of unique reflections	14880 (1022)	13281 (977)	3557 (193)
R_{merge} (%)	0.096 (1.019)	0.063 (1.544)	0.076 (1.283)
$R_{p.i.m.}$ (%)	0.024 (0.325)	0.015 (0.441)	0.019 (0.336)
$\langle I/\sigma(I) \rangle$	14.9 (1.2)	24.8 (1.6)	24.8 (1.7)
CC (1/2)	0.998 (0.620)	1.000 (0.672)	0.999 (0.743)
Completeness (%)	96.9 (91.8)	100.0 (100.0)	89.5 (71.9)
Overall *B* factor from Wilson plot ($Å^2$)	47.75	54.71	105.76

Anomalous Completeness	95.5 (89.9)	99.8 (100.0)	84.8 (68.1)
Anomalous Multiplicity	7.3 (5.0)	8.8 (6.6)	8.8 (7.0)

Table 2. Refinement.

	L18pI-Phe	L19pI-Phe	K20pI-Phe
PDB Code	6OWX	6OWZ	6OWY
Resolution range (Å)	42.79 - 2.06 (2.134 - 2.06)	42.43 - 2.05 (2.123 - 2.05)	42.26 - 2.07 (2.144 - 2.07)
Completeness (%)	99.89 (99.87)	99.94 (100.00)	99.65 (99.70)
CC 1/2	1 (0.651)	0.999 (0.861)	0.999 (0.691)
CC*	1 (0.888)	1 (0.962)	1 (0.904)
No. of reflections, working set	15669 (1516)	16247 (1538)	15674 (1511)
No. of reflections, test set	996 (93)	976 (92)	939 (91)
Final R_{cryst}	0.2256 (0.3250)	0.2150 (0.2778)	0.2268 (0.3604)
Final R_{free}	0.2803 (0.3851)	0.2549 (0.2945)	0.2724 (0.4299)
No. of non-H atoms			
Protein	1373	1382	1403
Ion	15	13	13
Ligand	26	19	16
Water	42	62	58
Total	1456	1476	1500
R.m.s. deviations			
Bonds (Å)	0.011	0.015	0.013
Angles (°)	1.21	1.20	1.23

Average *B* factors (Å^2)	66.97	60.61	58.31
Protein	66.41	60.72	58.74
Ion	81.31	64.32	66.28
Ligand	87.39	92.81	55.76
Water	73.42	54.87	48.21
Ramachandran plot			
Most favoured (%)	95.91	95.68	94.71
Allowed (%)	3.51	3.70	4.71
Outlier (%)	0.58	0.62	0.58
Rotamer Outliers (%)	0.74	0.70	0
Molprobity Clashscore	8.89	7.80	4.17
Molprobity score	1.76	1.73	1.56

Table 3: Peak heights detected for zinc and chlorine (in σ), from the 2.87 and 2.75 keV phased anomalous difference Fourier maps of the best L19pI-Phe Spy:Im7 crystal (labelled according to PDB Code 6OWZ). At 2.87 keV, Cl f" = 3.98, Zn f" = 4.0. At 2.75 keV, Cl f" = 0.43, Zn f" = 4.4 (Fig. S2).

Atom	***2.87 keV Peak Height***	***2.75 keV Peak Height***
Zn 1	3.6	5.6
Zn 2	4.6	5.0
Zn 3	5.0	6.1
Zn 4	4.2	4.7
Zn 5	5.3	7.8
Zn 6	6.9	9.6
Zn 7	14.0	10.8

Cl 1	12.0	0.3
Cl 2	11.0	1.1

Table 4: Iodine anomalous peak heights (in σ), occupancies and B-factors (Å^2) approximated from repeated refinements (Figure 2) for the best crystal of each Spy:Im7 complex at 5.2 keV.

Spy:Im7	***Peak Height***	***Occupancy***	***B-Factor***
L18pI-Phe	26.4	~0.20	~47
L19pI-Phe 1	8.9	~0.31	~87
L19pI-Phe 2	9.8	~0.49	~164
L19pI-Phe 3	6.3	~0.27	~106
L19pI-Phe 4	6.4	~0.12	~80
K20pI-Phe	32.5	~0.33	~55

3.2. L19pI-Phe demonstrates multiple binding poses of Im7 on Spy

From the three peptides tested, phased anomalous difference Fourier maps of L19pI-Phe show the highest number of anomalous signals that we can attribute to iodine. In addition to the anomalous density attributed to zinc, chlorine, and methionine, there are four distinct anomalous signals above 6 *σ* in the phased anomalous difference Fourier maps at 5.2 keV (Fig. 1*A* and Table 4). Of these four peaks, three (iodine number 1, 2, and 4) are very well validated by additional maps, as discussed below, whereas the remaining peak is less well supported (Fig. 1*C*).

When refined from many different starting values for occupancies and atomic displacement factors (Langan *et al.*, 2018) to estimate occupancies and temperature factors for these atoms, these iodines displayed both low occupancy and high temperature factors, with occupancies estimated to range from 0.12 to 0.49, and *B* factors ranging from 80 to 164 Å^2 (Fig. 2 and Fig. S4).

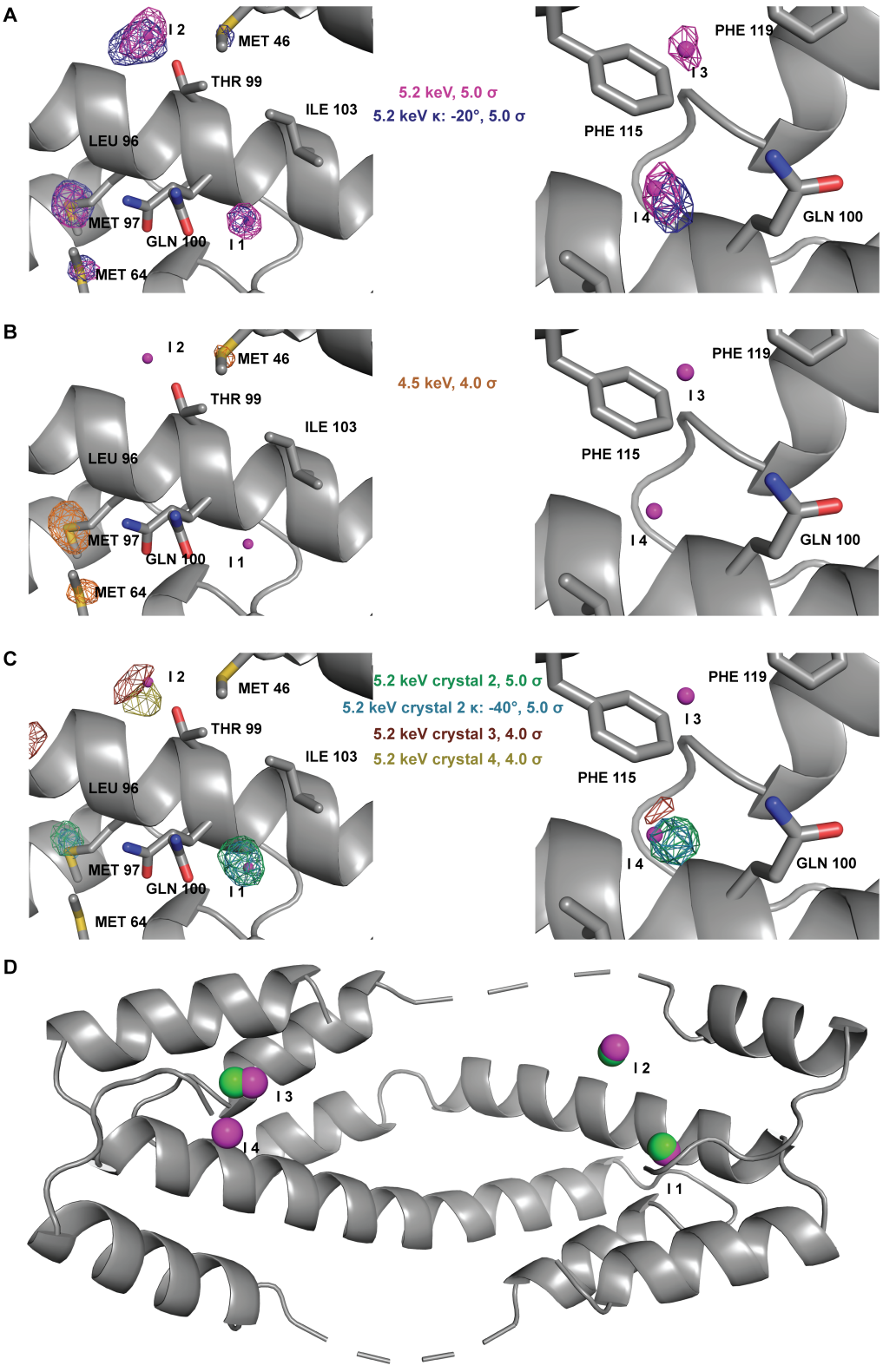

Figure 1

Phased anomalous difference Fourier maps and positions of the four iodine signals in L19pI-Phe crystals, displayed as purple spheres in each panel. Named and numbered residues are from Spy, whereas the partially occupied iodines are labeled with I. (A) Phased anomalous difference Fourier maps from 5.2 keV data collected at two different goniometer kappa angles, contoured at 5.0 σ. (B) Phased anomalous difference Fourier map from 4.5 keV contoured at 4 σ. (C) Phased anomalous difference Fourier maps from

data collected from different crystals, contoured at 5.0 σ (crystal 2) and 4 σ (crystal 3 and 4). (D) Overlap of L19pI-Phe iodine positions (magenta) detected here with closest iodine signals from previous data (green) (Horowitz *et al.*, 2016).

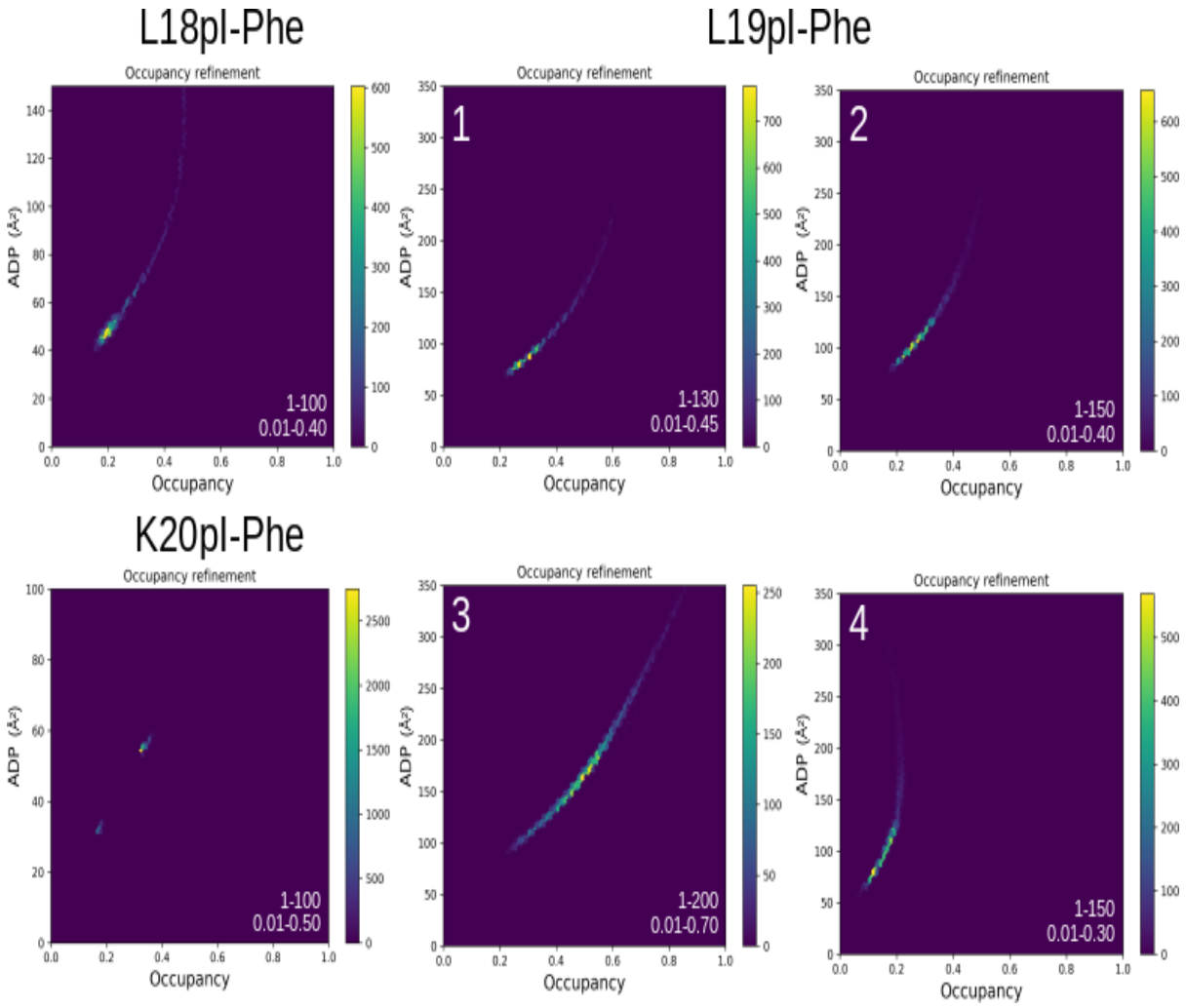

Figure 2

2D histogram showing occupancy refinement of the iodine positions in the three structures L18pI-Phe (6OWX), L19pI-Phe (6OWZ) and K20pI-Phe (6OWY) after 50 rounds of refinement from 10,000 randomly assigned APD/occupancy starting values (shown in Fig. S3). The color scale represents the number of structures in the bin. The starting value ranges for ADP and occupancy are shown in the bottom right corner of each plot.

To check if these signals are attributable to iodine, we collected an additional dataset on the same crystal at 4.5 keV, below the iodine L edges. At this energy, we would expect that the anomalous signal derived from iodine would dramatically decrease, whereas the change in anomalous signal from methionine, zinc, and chlorine would be negligible. The phased anomalous difference Fourier maps from this energy confirm that the non-iodine scatterers continue to display strong anomalous signals, whereas the signals from the four putative iodines disappear (Fig. 1B). This experiment indicates that the four anomalous signals are from the Im7 peptides and not from other anomalous scatterers. Moreover, the high σ values of the anomalous signals, the smallest of which was detected at 6.3 σ, make it unlikely that these signals represent noise. As a counterexample, the highest peaks not attributable to known anomalous scatterers, which hence could be noise, have σ values of

4.2 in the same map (Fig. S5A). However, a rigorous way to exclude the possibility that the anomalous signals do represent noise would be to determine if they are present in the same positions in an additional dataset collected at the same energy (at 5.2 keV) but using a different goniometer κ angle ($\kappa = -20^\circ$). Anomalous signals that appear in the same positions are highly likely to be true anomalous signals. It is worth mentioning that after a complete set of data, the intensity of the anomalous signal will decrease due to radiation damage. Therefore, only the signals with the highest intensity are detected after multiple additional data collections on the same crystal. The phased anomalous difference Fourier maps from this additional data collection show that three of the anomalous positions from the first data collection are preserved in the data collected at the different κ angle (Fig. 1A).

Finally, to test whether these anomalous positions are reproducible in other L19pI-Phe crystals, we collected additional 5.2 keV datasets from three other L19pI-Phe crystals. These crystals diffracted to resolutions of 2.2, 2.9, and 3.2 Å, respectively. In the phased anomalous difference Fourier map of the crystal that diffracted to 2.2 Å, we were able to identify three different iodine signals that overlap with signals detected in the highest resolution crystal (Fig. 1C). These signals were also present in other data collections ($\kappa = -40^\circ$) on the 2.2 Å diffracting crystal (Fig. *1C*). In the crystals that diffracted to 2.9 and 3.2 Å, we only detected one iodine signal in each, but they overlapped well with the strongest anomalous signal from the highest resolution crystal. It is therefore clear that the ability to detect low intensity signals is highly dependent on the crystal quality, as the best diffracting crystals showed the most high quality anomalous signals.

To further examine the anomalous peaks detected here, we also compared these iodine positions to those identified in our previous Spy-Im7 crystallography study in which we had used the same L19pI-Phe peptides with H96L Spy. We found that three of the four iodine anomalous positions detected here were also detected and used in our previous analysis (Fig. 1D).

The lowest L19pI-Phe anomalous peak (6.3 σ at 5.2 keV) is not present in the anomalous dataset from the crystals diffracting to lower resolution. However, this signal is very close (1.3 Å) to an L19pI-Phe anomalous peak observed in our previous Spy-Im7 crystallography study (Fig. 1D). So, although this peak was not well supported by additional datasets within this study, it was detected in our previous study.

3.3. Other Im7 peptides suggest additional Im7 binding sites in the crook of Spy's cradle

The Im7 L18pI-Phe and K20pI-Phe peptides crystallized in complex with Spy show a very different pattern compared to the multiple signals observed for L19pI-Phe. The 5.2 keV phased anomalous difference Fourier maps of 18pI-Phe and 20pI-Phe each show only one distinct anomalous signal attributable to iodine. In both cases, the peak heights in the phased anomalous difference Fourier maps were very strong; the iodine signals were detected at 26.4 and 32.5 σ for L18pI-Phe and K20pI-Phe, respectively (Figs. 3 and 4, and Table 4). Both peaks are on the interior of Spy's cradle, near the flexible loop region.

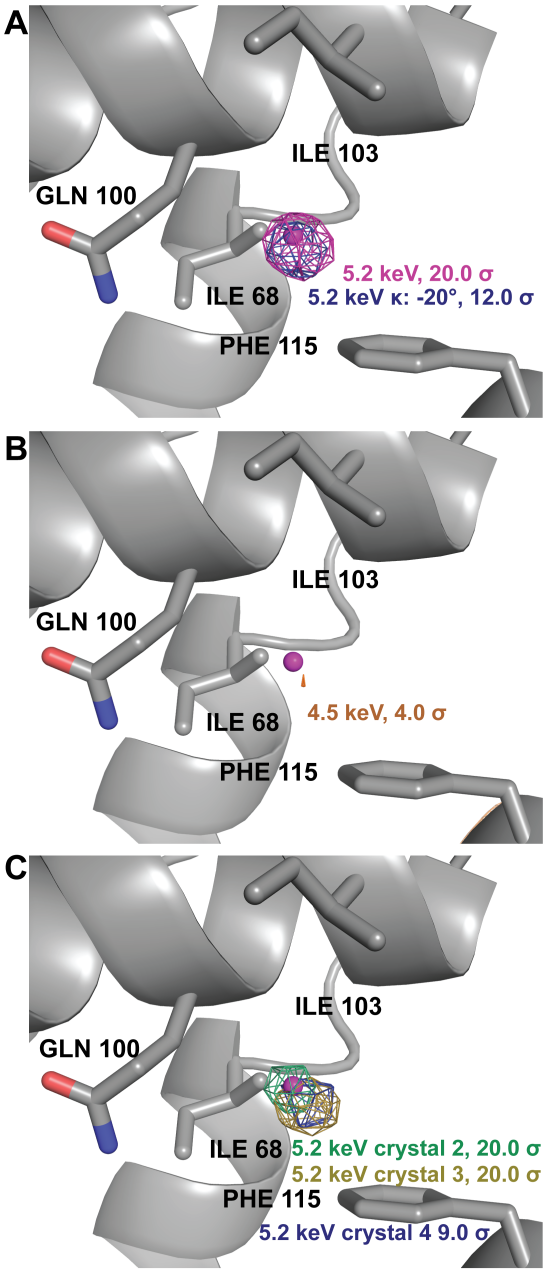

Figure 3

K20pI-Phe phased anomalous difference Fourier maps, with iodine atom depicted as a magenta sphere. Named and numbered residues are from Spy. (A) Phased anomalous difference Fourier maps from 5.2 keV datasets collected at two goniometer kappa angles, contoured at 20 σ and 12 σ, respectively. (B) Phased anomalous difference Fourier map from data collected at 4.5 keV, contoured at 4.0 σ. (C) Phased anomalous difference Fourier maps from data collected at 5.2 keV from three additional crystals, contoured at 20 σ (crystal 2 and 3) and 9 σ (crystal 4).

For K20pI-Phe, a second dataset below the iodine edge at 4.5 keV was collected. The large decrease of the anomalous signal in this dataset confirmed that the position ascribed to iodine was indeed iodine (Fig. 3B). To further validate this observation, we collected a third dataset at an additional goniometer κ angle ($\kappa = -20^\circ$) above the iodine edge. This dataset again showed strong anomalous signal (16.1 σ in the phased anomalous difference Fourier map) at the same position (Fig. 3A), with the peak height reduced by radiation damage (Table S1). Finally, we collected datasets at 5.2 keV from three additional crystals

that showed strong anomalous signals in the same position (26.7, 26.0, and 6.5 σ in phased anomalous difference Fourier maps), demonstrating good reproducibility for this signal (Fig. 3C). Consistent with the L19pI-Phe data collections, the strength of the iodine anomalous signal detected is highly dependent on the crystal quality. This combination of measurements confirmed that K20pI-Phe produced detectable anomalous scattering from a single position in the crystal, providing the ideal case for determining the position of a partially occupied anomalous scatterer.

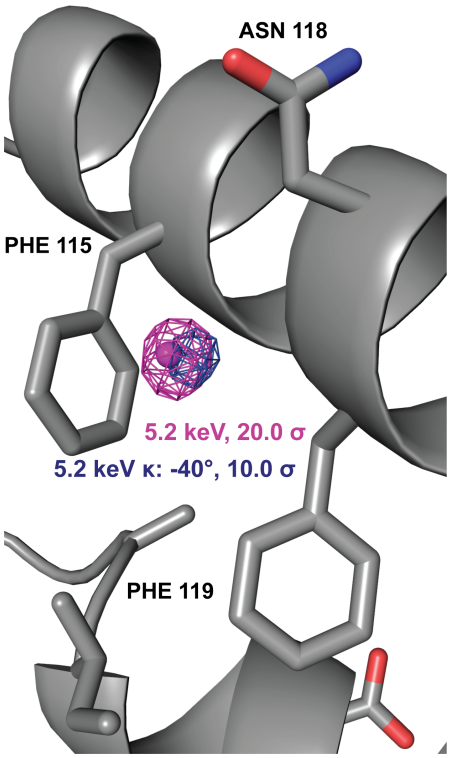

Figure 4
L18pI-Phe phased anomalous difference Fourier maps collected at 5.2 keV at two different goniometer κ angles, with iodine depicted as a magenta sphere. Named and numbered residues are from Spy.

Unfortunately, for L18pI-Phe, the single crystal that had diffraction adequate for anomalous analysis degraded during the second 5.2 keV dataset collections (Fig. 4 and Table 5). This dataset, collected at $\kappa = -40^{\circ}$, confirmed the presence of the anomalous signal (Fig. 4), but the 4.5 keV dataset could not be analyzed further due to radiation damage. However, other indicators strongly suggest that this *ANODE* anomalous peak also arises from iodine: (1) The height of the *ANODE* anomalous peak is the second largest observed in this study, and at 26.4 σ in the phased anomalous difference Fourier map, is substantially larger than the signals observed from zinc, chlorine, and methionine sulfur, the largest of which is 9.3 σ; (2) The position of this anomalous signal is structurally inconsistent with expected zinc or chlorine binding residues, which would be required to enable high enough occupancy binding to produce a strong anomalous signal. For example, this signal does not occur in the vicinity of zinc or chloride binding residues. So although the 4.5 keV dataset was not analyzed for this crystal, the strength of the signal and its chemical environment are inconsistent with it being derived from zinc or chloride, making it likely that the anomalous signal is due to the iodine in the Im7 peptide.

Further support for the L18pI-Phe signal coming from iodine derives from the observation that carbon-iodine bonds are labile and cleavage is expected to occur due to

radiation damage (von Schenck *et al.*, 2003; Zwart *et al.*, 2004; Koch *et al.*, 2011; Ennifar *et al.*, 2002), a feature previously exploited for phasing purposes (Schiltz & Bricogne, 2007; Zwart *et al.*, 2004). Thus, for anomalous signals of peptide-bound iodine, we would expect to see a decrease in signal intensity as a function of increasing X-ray dose, as the iodine is cleaved from the phenyl sidechain. This trend is demonstrated not just for L18pI-Phe, but also for K20pI-Phe in Table 5.

Table 5: Radiation damage specifically affects the iodine anomalous signals. As data collection proceeds, the anomalous signals (in σ from phased anomalous difference Fourier maps) for both L18pI-Phe and L20pI-Phe drop while that of a nearby methionine sulfur are less affected.

Spy:Im7	***L18pI-Phe***		***K20pI-Phe***	
Residue	Met93	Iodine	Met93	Iodine
1st 5.2 keV dataset	4.5	26.4	4.9	32.5
2nd 5.2 keV dataset	4.0	10.6	4.2	16.1

Examining the radiation dosage, absorbed doses estimated for L18pI-Phe, L19pI-Phe and K20pI-Phe crystals are respectively 0.66, 1.35 and 1.43 MGy (Table S1), suggesting that these data are not substantially affected by radiation damage. The higher contribution to the cumulative absorbed dose is mostly due to the dose absorbed during the subsequent data collection at 4.5 keV (8.32 and 8.49 MGy for L19pI-Phe and K20pI-Phe, respectively). Therefore, the anomalous signal peak heights in the later datasets collected at 5.2 keV, in different crystal orientations, are definitively affected by the high cumulative dose during multiple and sequential data collection. The decrease in the anomalous signals observed in the latter datasets is consistent with specific radiation damage suffered by the crystal.

The larger peak heights of L18pI-Phe and K20pI-Phe, as compared to each of the L19pI-Phe peaks, suggest a higher level of occupancy at these positions. Anomalous site refinements show that the occupancies of L18pI-Phe and K20pI-Phe are approximately 20% and 33% with *B* factors of approximately 47 and 55, respectively (Table 4). Similarly, the area adjacent to the anomalous signals in L18pI-Phe and K20pI-Phe shows electron density in $2F_o - F_c$ and $F_o - F_c$ maps consistent with the presence of a partially occupied, disordered peptide (Fig. 5). Attempts to perform traditional model building using the residual L18pI-Phe and K20pI-Phe peptide density were unsuccessful due to the weak nature of the electron density, as well as its somewhat amorphous shape, likely due to multiple conformations within the peptide. This density, however, still shows greater residual peptide occupancy than the areas surrounding the multiple L19pI-Phe iodine anomalous peaks, where we failed to see density above background, consistent with the higher occupancy of the single L18pI-Phe and K20pI-Phe positions. Of note, the electron density for the L18pI-Phe and K20pI-Phe mutants has a substantially more defined shape and signal strength than that observed previously in other mutants (Horowitz *et al.*, 2016).

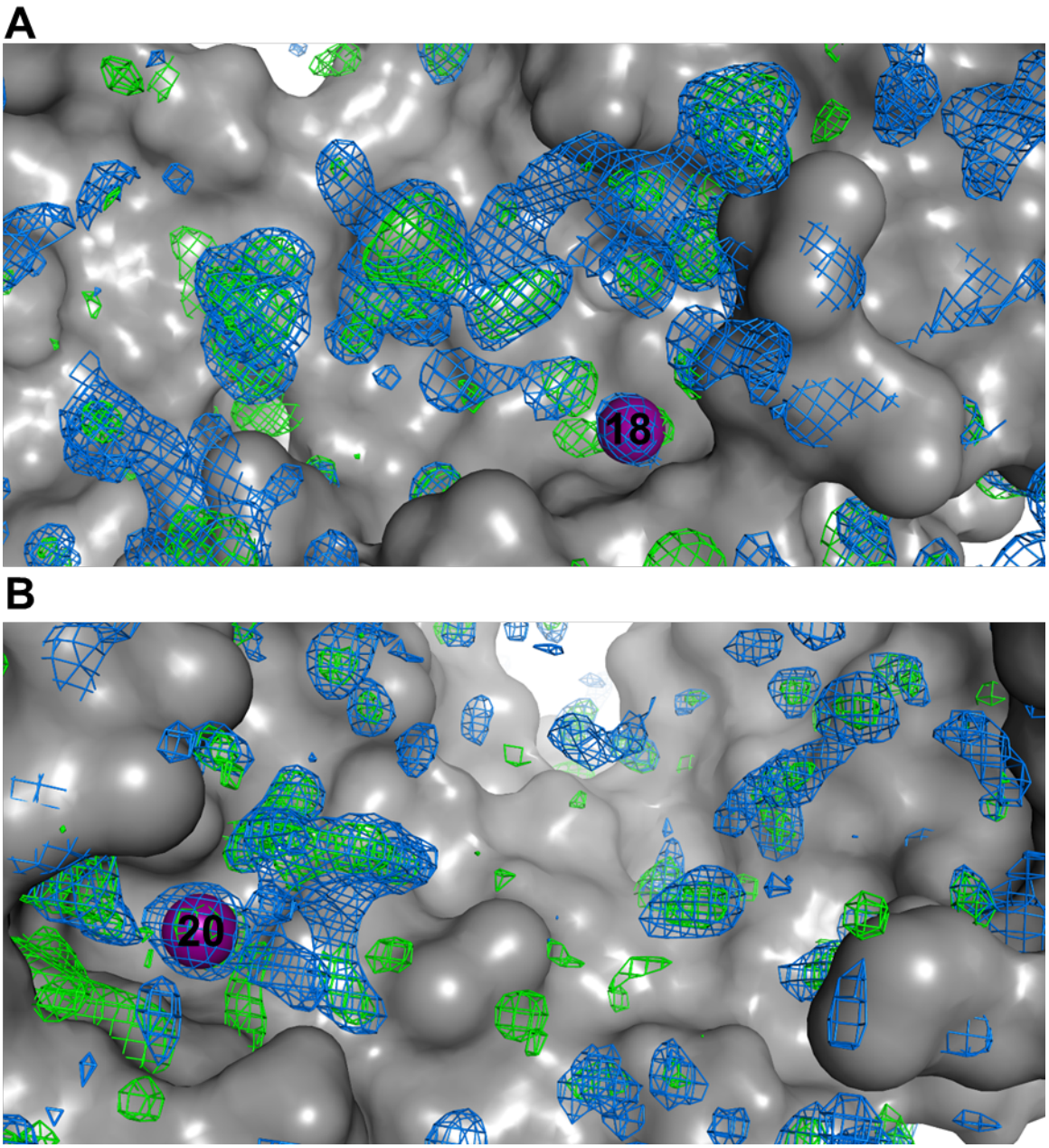

Figure 5
Residual electron density from disordered peptides. (A) L18pI-Phe peptide density. (B) K20pI-Phe peptide density. $2F_o - F_c$ map is displayed in blue, contoured at 0.6 σ, and $F_o - F_c$ map is displayed in green and red, contoured at 2.5 σ. Spy is shown as a gray surface. At this contour level, no negative $F_o - F_c$ density is visible in these regions.

3.4. READ selection using the novel datasets

The previously described READ selection method (Salmon *et al.*, 2018; Horowitz *et al.*, 2016) was applied by combining our previous datasets with the new data. For the most direct comparison, we substituted our previously recorded L19pI-Phe signals with the new corresponding data (Methods, Figure S9). On average, this procedure was able to fit the L19pI-Phe signals with an average error of 0.37 Å. The results from this selection are highly similar to the one previously obtained (Horowitz *et al.*, 2016), confirming the previously proposed ensemble. The improvement in the detection of L19pI-Phe signals also

translates into a higher contribution in the target function of the fitting procedure. Despite little rebalancing of the relative contribution of the data, the analysis leads to essentially the same ensemble (Fig. 6).

To investigate further the coherence of the two data sets, we tested how an ensemble determined with either the old or the new L19pI-Phe could predict the value from the other corresponding dataset. Using all of the old data (Horowitz *et al.*, 2016), the new four L19pI-Phe signals presented here could be predicted with an average deviation of 0.85 Å. Replacing the old L19pI-Phe signals with the new signals, the old L19pI-Phe signals were back-predicted with an associated error of 0.89 Å on average (only one signal was reproduced with an error of 3.9 Å while the other six could be predicted within 0.41 Å in average). This cross-validations procedure shows that the selections run using either the new or old L19pI-Phe signals can reproduce all signals in the other dataset, with the exception of one point of the old dataset, underlying the internal coherence of the data.

To further investigate the binding of Im7 into the surface of Spy, we additionally attempted selections using the L18pI-Phe and K20pI-Phe signals. In the case of L18pI-Phe, the MD simulation used to generate the conformational pool was found to not sample positions encompassing the iodine position in the crystal, preventing any fitting and further analysis of this signal (Figure S10). In this case, improving the conformational sampling in the MD will be required to fit this iodine position. In the case of K20pI-Phe, a simultaneous fitting of the new L19pI-Phe and K20pI-Phe within 0.43Å on average was possible. However, cross-validation tests in which the K20pI-Phe signal was held out did not back-predict the K20pI-Phe anomalous signal. This issue could have several sources: (i) the K20pI-Phe signal is providing unique information that is not present in the remaining of datasets (ii) the K20pI-Phe is not fully coherent with the remaining data due to changes induced by the amino acid substitution or (iii) the sampling in the initial conformational pool is inadequate to allow for this validation. In summary, the L19pI-Phe data is consistent with the previously characterized ensemble, while the L18pI-Phe and the K20pI-Phe data will require more advanced conformational sampling to properly assess their coherence with the determined ensemble.

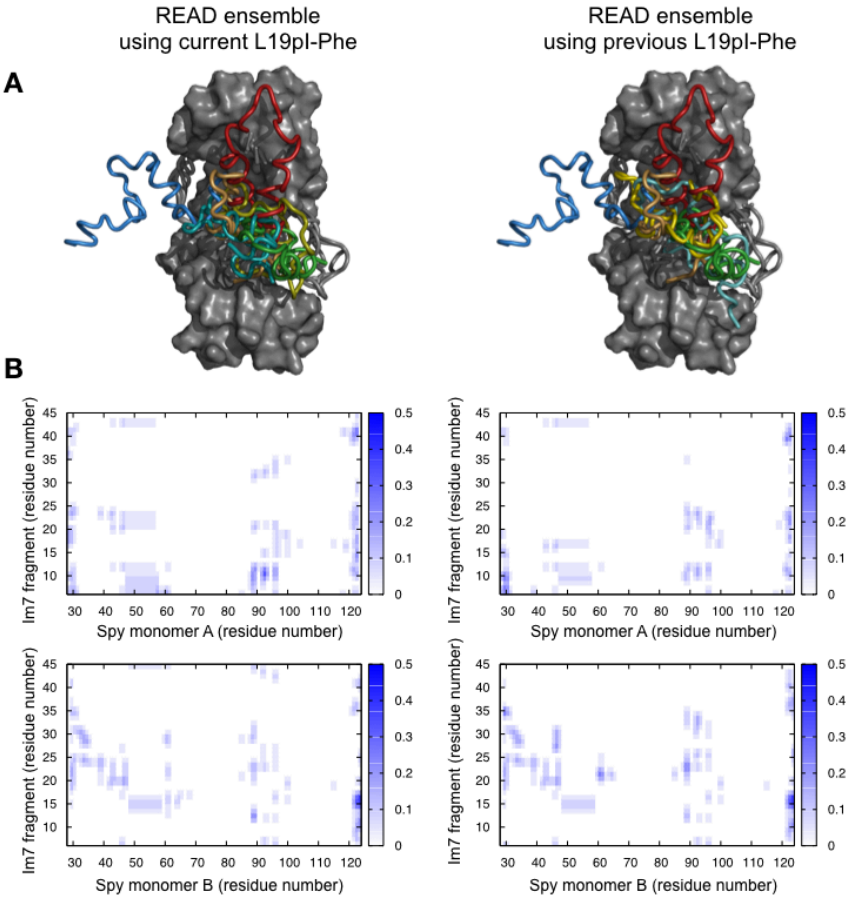

Figure 6
Comparison of the selected ensembles obtained using the current (left) and previous (right) L19pI-Phe datasets. For previously determined iodine positions, please see Fig. S10. (A) Comparison of the READ ensembles, including Spy (gray) and Im7 conformations (colors). (B) Contact map of the Im7-Spy interactions. The probability of contact increases from white to dark blue.

4. Discussion

Our new, optimized data collection strategy provides an improved method to obtain high quality anomalous signals with less noise contamination; it also verifies the presence of several of the iodine anomalous signals identified in our previous datasets. Combined, the experiments demonstrate that the Im7 peptide binds to Spy in multiple different binding poses, which are detectable using anomalous scattering. Refining the occupancies of the iodine suggests that we are able to detect iodine anomalous signals as low as ~12% occupancy, even with a high temperature factor of 80 Å^2. These lowly occupied states were confirmed via reproducibility through independent data collections at multiple angles and using separate crystals. The iodine positions are plausible, and in average located at around 3.25 Å from the closest atom (Table S2). READ selections demonstrated that the new L19pI-Phe data produced a consistent ensemble with previous efforts, while the consistency of the L18pI-Phe and K20pI-Phe could not be assessed properly with our initial sampling.

Spy-Im7 binding has recently received attention as a model system for understanding chaperone-client interactions. NMR spectroscopy, molecular dynamics simulations, chemical kinetics, and X-ray crystallography have all concluded that client binding to Spy is dynamic and that Im7 can bind to Spy in an array of conformations and poses (He & Hiller, 2018; He *et al.*, 2016; Stull *et al.*, 2016; Horowitz *et al.*, 2016). These studies showed that Im7 binding occurs at various sites on the concave surface of the Spy cradle. The work here confirms these findings and provides an avenue to identify binding sites directly at higher sensitivity than was previously possible.

The data reported here confirms that Im7 binds to Spy in multiple binding poses, as suggested by the interesting pattern of the anomalous signals (Fig. 7). The *ANODE* anomalous peaks for L18pI-Phe and K20pI-Phe are both very close to separate L19pI-Phe *ANODE* anomalous peaks. This proximity suggests a degree of promiscuity in the binding sites in which Im7 can shift small distances to accommodate pI-Phe binding. Moreover, based on the decreasing peak intensities of the iodine anomalous signals through the data collection (Table 5), we can rule out that these positions are iodine ions that have been cleaved from pI-Phe, as this would have produced the opposite trend. These positions are not equivalent, as no iodine density in L18pI-Phe is visible at the K20pI-Phe site, or vice-versa. These measurements confirm the observations that Im7 binds to Spy promiscuously, but with specific anchor points between Spy and Im7 (Horowitz *et al.*, 2016; He *et al.*, 2016).

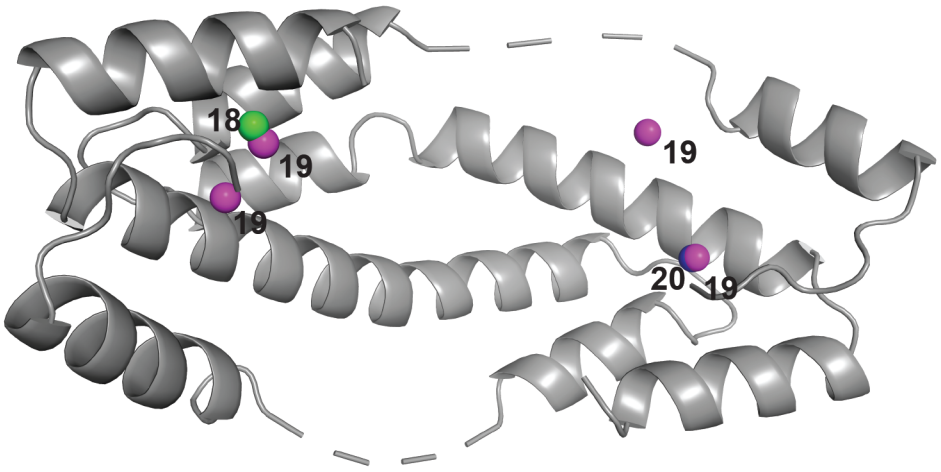

Figure 7
Iodine positions observed in this study, displayed in green (L18pI-Phe), magenta (L19pI-Phe), or blue (K20pI-Phe), respectively, and labeled by Im7 residue number.

Direct READ selections and cross-validations demonstrated that the new L19pI-Phe data produced a consistent ensemble with the previously-determined ensemble (Horowitz *et al.*, 2016). Further investigations will be needed to adequately incorporate the analysis of the L18pI-Phe and K20pI-Phe signal positions. At the very least, new methods for increasing the sampling in the initial conformational pool will be required to fit these signals.

In our previous publication (Horowitz *et al.*, 2016) on crystals of the Spy-Im7 complex, the anomalous data from the partially occupied Im7 conformations was criticized as being too noisy for analysis (Wang, 2018). In this study, we repeated the measurement of one of the mutants (L19pI-Phe) used in our previous study. Three of the four sites identified here for L19pI-Phe were also observed in our earlier, noisier data (Horowitz *et al.*, 2016). Although our previous cross-validation analyses demonstrated that even our earlier noisier anomalous data contained valuable information (Horowitz *et al.*, 2016; Horowitz, Salmon, *et al.*, 2018) about the Im7 conformations that could then be modeled, the sensitivity of the previously reported experiments was certainly a limiting factor in the technique. In the previous work, the data quality was limited by a combination of detector size and sensitivity due to the CCD detectors employed, as well as air scattering and absorption. The new long wavelength beamline I23 at Diamond Light Source enables the imposition of more stringent criteria for detection of weak anomalous signals. This approach should dramatically improve the ability to delineate disordered molecules in crystals.

Acknowledgements

The authors would like to thank C. Travaglini-Allocatelli and A. Di Matteo for useful conversations, Ke Wan for assistance with protein purification.

Funding information

This work was supported by the National Institutes of Health grant R00 GM120388. J.C.A.B. is a Howard Hughes Investigator.

References

Adams, P. D., Afonine, P. V., Bunkoczi, G., Chen, V. B., Davis, I. W., Echols, N., Headd, J. J., Hung, L. W., Kapral, G. J., Grosse-Kunstleve, R. W., McCoy, A. J., Moriarty, N. W., Oeffner, R., Read, R. J., Richardson, D. C., Richardson, J. S., Terwilliger, T. C. & Zwart, P. H. (2010). *Acta Crystallogr D Biol Crystallogr* **66**, 213-221.

Afonine, P. V., Grosse-Kunstleve, R. W., Echols, N., Headd, J. J., Moriarty, N. W., Mustyakimov, M., Terwilliger, T. C., Urzhumtsev, A., Zwart, P. H. & Adams, P. D. (2012). *Acta Crystallogr D Biol Crystallogr* **68**, 352-367.

Bury, C. S., Brooks-Bartlett, J. C., Walsh, S. P. & Garman, E. F. (2018). *Protein Sci* **27**, 217-228.

Emsley, P., Lohkamp, B., Scott, W. G. & Cowtan, K. (2010). *Acta Crystallogr D Biol Crystallogr* **66**, 486-501.

Ennifar, E., Carpentier, P., Ferrer, J. L., Walter, P. & Dumas, P. (2002). *Acta Crystallographica Section D-Biological Crystallography* **58**, 1262-1268.

Evans, P. R. & Murshudov, G. N. (2013). *Acta Crystallogr D Biol Crystallogr* **69**, 1204-1214.

Handing, K. B., Niedzialkowska, E., Shabalin, I. G., Kuhn, M. L., Zheng, H. P. & Minor, W. (2018). *Nature Protocols* **13**, 1062-1090.

He, L. & Hiller, S. (2018). *Angew Chem Int Ed Engl* **57**, 5921-5924.

He, L. C., Sharpe, T., Mazur, A. & Hiller, S. (2016). *Sci Adv* **2**.

Hendrickson, W. A. (2014). *Q Rev Biophys* **47**, 49-93.

Horowitz, S., Koldewey, P., Stull, F. & Bardwell, J. C. A. (2018). *Curr Opin Struc Biol* **48**, 1-5.

Horowitz, S., Salmon, L., Koldewey, P., Ahlstrom, L. S., Martin, R., Quan, S., Afonine, P. V., van den Bedem, H., Wang, L., Xu, Q., Trievel, R. C., Brooks, C. L., 3rd & Bardwell, J. C. (2016). *Nat Struct Mol Biol* **23**, 691-697.

Horowitz, S., Salmon, L., Koldewey, P., Ahlstrom, L. S., Martin, R., Quan, S., Afonine, P. V., van den Bedem, H., Wang, L., Xu, Q., Trievel, R. C., Brooks, C. L., 3rd & Bardwell, J. C. A. (2018). *Nat Struct Mol Biol* **25**, 990-991.

Kabsch, W. (2010). *Acta Crystallogr D Biol Crystallogr* **66**, 125-132.

Koch, C., Heine, A. & Klebe, G. (2011). *Journal of Synchrotron Radiation* **18**, 782-789.

Koldewey, P., Stull, F., Horowitz, S., Martin, R. & Bardwell, J. C. A. (2016). *Cell* **166**, 369-379.

Langan, P. S., Vandavasi, V. G., Weiss, K. L., Afonine, P. V., El Omari, K., Duman, R., Wagner, A. & Coates, L. (2018). *Nat Commun* **9**, 4540.

Pflug, A., Johnson, K. A. & Engh, R. A. (2012). *Acta Crystallogr F* **68**, 873-877.

Phillips, J. C., Wlodawer, A., Yevitz, M. M. & Hodgson, K. O. (1976). *P Natl Acad Sci USA* **73**, 128-132.

Quan, S., Wang, L., Petrotchenko, E. V., Makepeace, K. A., Horowitz, S., Yang, J., Zhang, Y., Borchers, C. H. & Bardwell, J. C. (2014). *Elife* **3**, e01584.

Salmon, L., Ahlstrom, L. S., Bardwell, J. C. A. & Horowitz, S. (2018). *Methods Mol Biol* **1764**, 491-504.

Schiltz, M. & Bricogne, G. (2007). *Journal of Synchrotron Radiation* **14**, 34-42.

Stull, F., Koldewey, P., Humes, J. R., Radford, S. E. & Bardwell, J. C. A. (2016). *Nat Struct Mol Biol* **23**, 53-58.
Thorn, A. & Sheldrick, G. M. (2011). *J Appl Crystallogr* **44**, 1285-1287.
Venditti, V., Egner, T. K. & Clore, G. M. (2016). *Chem Rev* **116**, 6305-6322.
von Schenck, H., Weissenrieder, J., Helldén, S., Åkermark, B. & Göthelid, M. (2003). *Applied Surface Science* **212-213**, 508-514.
Wagner, A., Duman, R., Henderson, K. & Mykhaylyk, V. (2016). *Acta Crystallogr D Struct Biol* **72**, 430-439.
Wang, H., Elferich, J. & Gouaux, E. (2012). *Nat Struct Mol Biol* **19**, 212-219.
Wang, J. (2018). *Nat Struct Mol Biol* **25**, 989-990.
Zwart, P. H., Banumathi, S., Dauter, M. & Dauter, Z. (2004). *Acta Crystallogr D* **60**, 1958-1963.